

Check for updates

# An Integrated Engineered Bacterial Nanocomposite System for Targeted Prodrug Delivery and Enhanced Antitumor Efficacy

Yuqi Li, Lihui Ren, Hui Li, Zhengwei Xu, Muhan Chen, Jun Yang, Zixuan Wang, Jiawei Yuan, Shangwen Zhang, Shu Wei, Jiayun Xu, Dingcheng Zhu, Hongcheng Sun, Junqiu Liu,\* and Shuangjiang Yu\*

Even with the promising therapeutic potential of engineered bacteria that target tumors, effective cancer treatment will still need to involve combination strategies. Herein, a model strain of Escherichia coli (BL21) is aimed to engineer to internally produce copper sulfide nanoparticles (CuS), which are subsequently armed with disulfiram-loaded gold nanorods, resulting in Au-DSF@CuS-BL21 for hypoxic-targeted prodrug delivery and enhanced antitumor effects. The bacterial membrane in this system serves as a barrier between the prodrugs of CuS and DSF, preventing the premature formation and release of the highly toxic CuET complex during circulation, thus ensuring bacterial survival and minimizing drug leakage. The key findings revealed that bacterial activity of Au-DSF@CuS-BL21 is effectively sustained, exhibiting enhanced capabilities for tumor targeting and penetration. Upon activation by 808 nm near-infrared laser irradiation, photothermal bacterial lysis is induced, resulting in the release of CuS and DSF. This process facilitate the formation of the highly toxic CuET complex, as well as augmented antitumor efficacy by stimulating the innate immune response. Collectively, these findings offer promising opportunities for enhancing the biosafety of modified bacteria, as well as for compartmentalized prodrug delivery and improved effectiveness of combination antitumor therapies.

#### 1. Introduction

Increasing the target efficiency of therapeutic agents while minimizing systemic side effects is the central objective in the field of anticancer drug delivery.<sup>[1]</sup> The unique physiological features of

Y. Li, L. Ren, H. Li, Z. Xu, M. Chen, J. Yang, Z. Wang, J. Yuan, S. Zhang, S. Wei, J. Xu, D. Zhu, H. Sun, J. Liu, S. Yu

Key Laboratory of Organosilicon Chemistry and Material Technology Ministry of Education

College of Material

Chemistry and Chemical Engineering Jing Hengyi School of Education

Hangzhou Normal University Hangzhou 311121, China

E-mail: junqiuliu@jlu.edu.cn; yusj@hznu.edu.cn

The ORCID identification number(s) for the author(s) of this article can be found under https://doi.org/10.1002/adfm.202519382

DOI: 10.1002/adfm.202519382

solid tumors offer a vital opportunity to achieve this objective. [2] For example, hypoxia has emerged as a pivotal physiological characteristic of the solid tumor microenvironment (TME), suggesting novel avenues for the formulation of targeted tumor treatment strategies. [3–5]

Obligate anaerobes and facultative anaerobes thrive in hypoxic tumor regions, creating potential hypoxic-targeted vehicles for efficient drug delivery and cancer treatment.[6-10] Its modifiable surface allows the attachment of small-molecule drugs and nanotherapeutics to enhance targeted in vivo delivery.[11] Genetic engineering enables bacteria to express therapeutic proteins and particles, producing specific effects.[12-16] In addition, parts of bacteria can influence antitumor immune responses both systemically and in the TME, presenting a promising opportunity to integrate live bacteria with other immunotherapy strategies.[17,18] These features make genetically engineered bacteria promising carriers for cancer combination therapy.[19] However, the absence of selectivity in some

cytotoxic drugs results in the inactivation of bacterial vehicles, presenting a significant challenge for their delivery using live bacteria. [20,21] Expectedly, employing tumor-targeting bacteria to deliver non-toxic or low-toxicity prodrugs to the tumor location, then activating them to produce highly cytotoxic therapeutic agents, could offer valuable insights into addressing the previously mentioned challenges. [22-24]

Disulfiram (DSF) was initially employed to treat alcoholism and has since been found to possess anticancer properties by converting into a highly cytotoxic diethyldithiocarbamate-copper complex (CuET) when combined with copper ions (Cu<sup>2+</sup>).<sup>[25-27]</sup> The main challenge in improving the treatment strategy involving DSF and Cu<sup>2+</sup> lies in the poor water solubility and stability of DSF, the uneven distribution of copper ions in the body, and the absence of specific tumor characteristics.<sup>[28]</sup> Therefore, developing a safe and efficient method to efficiently deliver DSF and Cu<sup>2+</sup> to tumor sites to induce cytotoxicity is crucial for enhancing the effectiveness of this treatment.

1616328, D. Downloaded from https://advanced.onlinelibrary.wiley.com/doi/10.1002/adfm.202519382 by Hangzhou Normal University, Wiley Online Library on [10/11/2025]. See the Terms and Conditions (https://onlinelibrary.wiley.com/terms-and-conditions) on Wiley Online Library for rules of use; OA articles are governed by the applicable Creative Commons License

Given the challenges outlined above, this study developed a compartmentalized prodrug delivery strategy utilizing a bacteriamediated nanocomposite system (Au-DSF@CuS-BL21) to minimize the side effects of therapeutic agents while enhancing their antitumor efficacy. Initially, genetically engineered BL21 was used as a host strain to biosynthesize and deliver copper sulfide nanoparticles (CuS). Then, DSF-loaded polyethylene glycolthiol ether (mPEG-SH)-modified gold nanorods (AuNRs) were fixed to the surface of the bacteria via the dopamine (DA) deposition method. This bacteria-derived drug delivery system is designed to migrate to the tumor site via hypoxia targeting and facilitate the release of DSF from the AuNRs in the slightly acidic microenvironment of tumors. Upon exposure to near-infrared laser (NIR, 808 nm) irradiation, the AuNRs generate photothermal effects, which not only induce cytotoxicity in tumor cells but also lead to photothermal lysis of BL21, resulting in the accelerated release of therapeutic payloads. The released CuS nanoparticles not only exhibit photothermal properties but also simultaneously produce and release Cu<sup>2+</sup> under NIR irradiation. The generated Cu2+ ions immediately bind with DSF to form the highly cytotoxic CuET, which promotes intratumoral immunogenic cell death (ICD), thereby enhancing immune responses and yielding a synergistic antitumor efficacy. [29] This strategy reveals promising opportunities for improving the biosafety of engineered bacteria, in addition to compartmental prodrug delivery and improved antitumor efficacy (Scheme 1).

# 2. Results and Discussion

#### 2.1. Preparation and Characterization of Au-DSF

AuNRs have gained significant attention in the field of antitumor drug delivery and therapeutic investigations because of their tunable dimensions, facile surface modification capabilities, and superior photothermal properties in the NIR region.<sup>[30–32]</sup> Herein, a two-step growth method involving the use of seeds and hydroquinone as a reducing agent was employed to synthesize AuNRs with photothermal conversion capabilities in the NIR I region. This choice aims to balance the potential photothermal effects of CuS nanoparticles in the following study.[33] As shown in Figure 1A and Figures S1 and S2 (Supporting Information), three distinct types of AuNRs, designated AuNRs-1, AuNRs-2, and AuNRs-3, were successfully synthesized by varying the concentration of silver nitrate in the growth solution. TEM images and statistical analysis of nanomeasurements confirmed the successful production of AuNRs with different aspect ratios. Additionally, UV-vis-NIR spectroscopy revealed a shift in the longitudinal localized surface plasmon resonance (LSPR) peak from 780 to 931 nm and 1014 nm, corresponding to the different aspect ratios. Upon irradiation with an 808 nm laser, the temperature of AuNRs-1 increased to over 60 °C within 5 min, demonstrating superior photothermal performance compared with that of the other two samples (Figure S3, Supporting Information). Importantly, the characteristic absorption peak of AuNRs-1 is closely aligned with the 808 nm wavelength, akin to the absorption characteristics of CuS nanoparticles, which may enhance their combined photothermal efficacy.[34] Consequently, AuNRs-1 were selected for further investigation in subsequent studies.

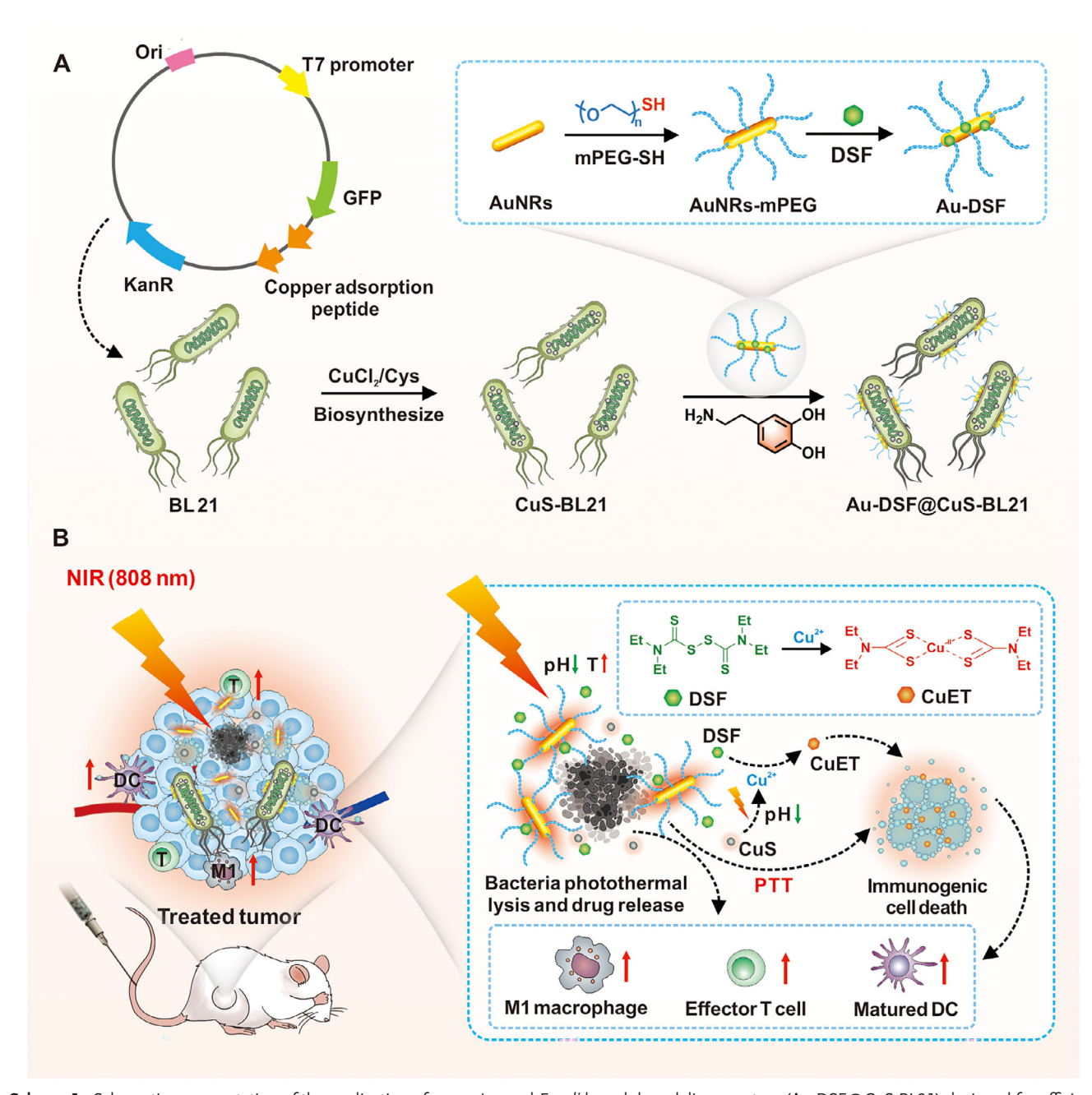
The surfaces of the AuNRs were subsequently modified with mPEG-SH (AuNRs-mPEG) to ensure effective dispersion of the nanorods. Following this modification. DSF was anchored onto the AuNRs-mPEG via sulfur-gold bonds, resulting in the formation of DSF-loaded mPEG-SH-modified AuNRs (Au-DSF). As illustrated in Figure 1B, no significant changes in the peak absorption or position of Au-DSF were observed compared with those of the unmodified AuNRs, suggesting that the incorporation of mPEG-SH and DSF does not obviously alter the local surface plasmon resonance of the AuNRs. Furthermore, the characteristic absorption peak of DSF at 267 nm was observed, confirming the successful absorption of DSF onto the surface of the AuNRs. Moreover, the zeta potentials of AuNRs, AuNRs-mPEG, and Au-DSF were measured to be  $28.1 \pm 7.4$ ,  $-9.6 \pm 1.0$ , and  $20.5 \pm 4.3$ mV, respectively, further supporting the adsorption of mPEG and DSF onto the surface of the AuNRs (Figure 1C). As shown in Figure 1D, elemental mapping analysis demonstrated that sulfur was uniformly distributed across the surface of the AuNRs in the Au-DSF sample. Conversely, a less pronounced sulfur signal was detected in the AuNRs-mPEG, suggesting a greater sulfur concentration in the Au-DSF, which can likely be attributed to the incorporation of DSF. Additionally, we investigated the stability and release properties of DSF at three different pH levels to replicate normal physiological conditions (pH = 7.4), TME (pH = 6.5), and lysosomal environments (pH = 5.0) following its application to the surface of AuNRs. Inductively coupled plasma (ICP) analysis revealed that the loading capacity of DSF within the AuNRs reached ≈10%, whereas the cumulative release in PBS at pH 7.4 was only 4.6% over a 48-h period. These findings suggest that both DSF and the AuNRs maintain good stability in a normal physiological environment, which is advantageous for the safe in vivo delivery of DSF. Upon reducing the pH to 6.5, there was a notable increase in the release rate of DSF, with the cumulative release reaching 54.7% after 48 h. Moreover, the release rate under NIR irradiation increased to 61.6% at pH 5.0. This phenomenon can be attributed to the diminished electrostatic interactions between DSF and the AuNRs, which are compromised by the presence of a positive charge in acidic environments (Figure 1E). Additionally, NIR treatment markedly enhanced the release of DSF, particularly at pH values of 7.4 and 6.5. This effect is likely due to the increased thermal motion of molecules at elevated temperatures, which weakens the gold-sulfur interaction and leads to increased DSF release. This pH- and photothermally responsive mechanism of DSF release is crucial for the effective delivery of DSF in subsequent tumor therapy studies.

#### 2.2. Formulation and Analysis of Au-DSF@CuS-BL21

Some microorganisms, including bacteria and fungi, can metabolize copper ions and sulfide ions into CuS nanoparticles. [35] These nanoparticles have demonstrated considerable promise for use in antitumor therapy, positioning them as novel therapeutic nanomaterials. [36] Herein, BL21 is utilized as the host strain model for the development of copper-resistant bacterial strains (CuS@BL21) owing to its strong protein expression capacity under the defined experimental conditions. A plasmid that incorporates a Cu<sup>2+</sup>-binding peptide was constructed on the basis of previous studies (Figure S4, Supporting Information). [37,38] This

onlinelibrary.wiley.com/doi/10.1002/adfm.202519382 by Hangzhou Normal University, Wiley Online Library on [10/11/2025]. See the Terms

) on Wiley Online Library for rules of use; OA articles are governed by the applicable Creative Commons



Scheme 1. Schematic representation of the application of an engineered *E. coli*-based drug delivery system (Au-DSF@CuS-BL21) designed for efficient antitumor therapy. Preparation process (A) and underlying antitumor mechanism (B) of Au-DSF@CuS-BL21.

plasmid included a green fluorescent protein to evaluate the expression of the affinity peptide and to enable further characterization. Then, endotoxin-free BL21 was employed as the expression system for the  $\text{Cu}^{2+}$ -binding peptide, enabling the conversion of CuS nanoparticles within a copper-rich environment.

To support bacterial survival and achieve the optimal concentration of CuS nanoparticles, 4 specific ratios of  $Cu^{2+}$  to cysteine were selected for the bacterial growth medium, as shown in Figure S5 (Supporting Information). The optimal  $Cu^{2+}$ -tocysteine ratio was found to be 1:4 on the basis of bacterial growth and precipitation analysis with different shaking durations. The

assessment of the bacterial mixture and precipitate, as depicted in Figure S6A (Supporting Information), along with the results from the confocal live/dead bacterial staining presented in Figure S6B (Supporting Information), indicated that BL21 exhibited optimal viability in the Cu<sup>2+</sup>-enriched medium for a duration of 5 h; however, viability declined significantly after 12 h. The concentration of CuS nanoparticles within *E. coli* was quantified using ICP analysis. As shown in Figure S7 (Supporting Information), the copper content within BL21 increased with increasing shaking time, although minimal changes were observed after the 5 h mark. Considering the survival of bacteria and the amount of

16163028, 0, Downloaded from https://advanced.onlinelibrary.wiley.com/doi/10.1002/adfm.202519382 by Hangzhou Normal University, Wiley Online Library on [10/11/2025]. See the Terms

and Conditions (https://onlinelibrary.wiley.com/ten

-conditions) on Wiley Online Library for rules of use; OA articles are governed by the applicable Creative Commons License

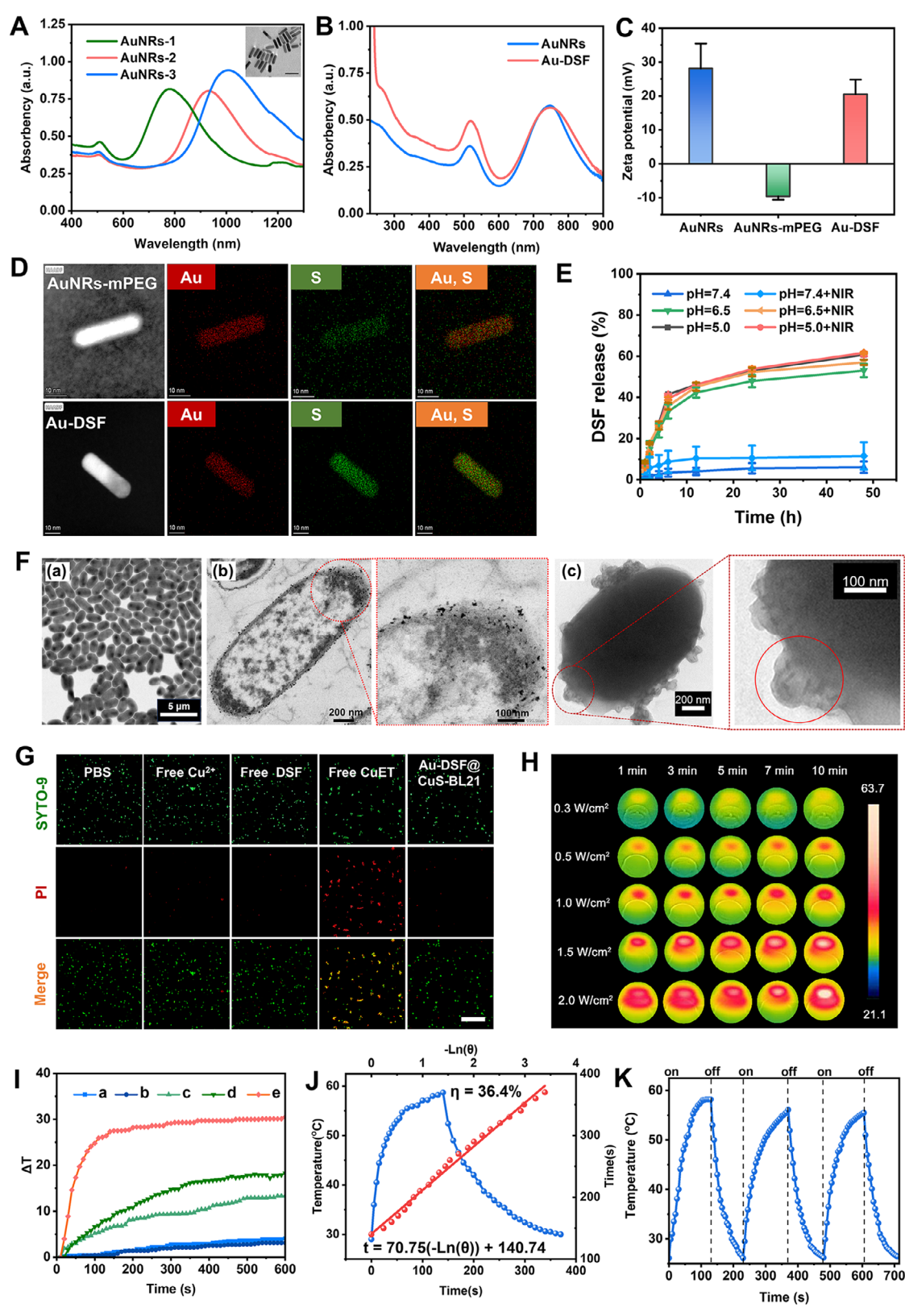


**Figure 1.** Characteristics of Au-DSF. A) UV-vis spectra of three types of AuNRs with different aspect ratios. B) UV-vis spectra of free AuNRs and Au-DSF. C) Zeta potential diagrams of the AuNRs, AuNRs-mPEG, and Au-DSF (n = 3). D) Elemental mapping images of the sulfur in AuNR-mPEG and Au-DSF (scale bar, 10 nm). E) DSF release curves from Au-DSF under different conditions (n = 3). F) Representative TEM image of CuS-BL21 (a), bright-field STEM images of CuS nanoparticles within CuS-BL21 (b), and TEM images of Au-DSF@CuS-BL21 (c). G) CLSM images of bacterial viability after exposure

1616328, D. Downloaded from https://advanced.onlinelibrary.wiley.com/doi/10.1002/adfm.202519382 by Hangzhou Normal University, Wiley Online Library on [10/11/2025]. See the Terms and Conditions (https://onlinelibrary.wiley.com/terms-and-conditions) on Wiley Online Library for rules of use; OA articles are governed by the applicable Creative Commons License

copper present, the optimal culture conditions for copperresistant bacteria were determined, and we set the concentrations of Cu<sup>2+</sup> and cysteine at 3.0 and 12.0 mm, respectively, with a shaking period of 5 h. Under the optimized conditions mentioned above, it is clear that biosynthesized CuS particles are located within the gaps of the bacterial membrane, indicating the successful isolation of CuS@BL21 (Figure 1F; Figure S8, Supporting Information). Moreover, experiments investigating the release of Cu<sup>2+</sup> from CuS@BL21demonstrated that laser irradiation at 808 nm facilitates a more efficient release of Cu<sup>2+</sup> compared to irradiation at 980 and 1064 nm (Figure S9, Supporting Information). This wavelength corresponds closely with the characteristic absorption peak of AuNRs-1, thereby corroborating the in situ generation of CuET.

Thereafter, Au-DSF was conjugated to the surface of CuS@BL21 through the process of DA co-deposition, following standard methodologies with slight modifications.[39,40] The TEM image presented in Figure 1F illustrates the successful development of an engineered bacterial strain, designated Au-DSF@CuS-BL21, which displays Au-DSF on its surface. The bacterial activity of the obtained Au-DSF@CuS-BL21 was subsequently verified by a live/dead bacterial staining assay. As shown in Figure 1G, most bacteria remained viable when exposed to Cu<sup>2+</sup> or DSF for the given time; in contrast, a substantial number of bacteria became nonviable in the presence of the CuET solution. However, the bacterial survival rate of the Au-DSF@CuS-BL21 group clearly improved compared with that of the CuET-treated group, suggesting that the strategy of compartmentalized CuS and DSF delivery can significantly protect the activity of bacterial vehicles.

# 2.3. Evaluation of Photothermal Properties

Extensive research on the photothermal conversion of AuNRs has led to their use in cancer therapies, where they absorb light of specific wavelengths and convert it into heat to destroy tumor cells.[41,42] Similarly, the photothermal properties of CuS nanoparticles have been studied, making them promising candidates for biomedical applications, particularly in cancer treatment.[43-45] Herein, the photothermal characteristics of BL21-derived formulations were examined under NIR irradiation (808 nm). As illustrated in Figure 11, the incorporation of polydopamine (PDA), CuS, or Au-DSF into the system markedly increased the photothermal temperature to different extents compared with that of free BL21. Furthermore, the simultaneous presence of all three factors results in the highest efficiency of photothermal enhancement, which is attributable to the superposition effect in the Au-DSF@CuS-BL21-treated group. Figure 1H and Figure \$10 (Supporting Information) also show that the temperature of the engineered bacteria can be adjusted by varying the concentration of Au-DSF and the intensity of laser irradiation. Moreover, a comprehensive assessment of the photothermal

conversion efficiency of Au-DSF@CuS-BL21 was conducted. As shown in Figure 1J, according to calculations, the photothermal conversion efficiency was 36.4%. Then, the cycling photothermal properties of Au-DSF@CuS-BL21 were thoroughly evaluated. Figure 1K illustrates three cycles of laser activation and deactivation, demonstrating consistent and stable temperature variations. In addition, we assessed the efficacy of CuS in BL21 by facilitating its reaction with DSF to yield CuET under NIR irradiation. The UV spectrum presented in Figure S11 (Supporting Information) reveals a characteristic peak for CuET at ≈265 and 450 nm, which suggests that the CuS nanoparticles biosynthesized in BL21 can effectively release Cu<sup>2+</sup> and undergo a chemical reaction with DSF to form CuET when exposed to NIR irradiation. Overall, these results demonstrate that Au-DSF@CuS-BL21 possesses good photothermal properties and NIR-mediated CuET generation, highlighting its potential applications in multimodal cancer therapy.

#### 2.4. Evaluation of Therapeutic Effects In Vitro

To ensure the survival and smooth transportation of drugs by engineered bacteria, the migration ability of engineered BL21 cells was first assessed using a transwell assay. Briefly, the bacteria were introduced into the upper chamber of the transwell apparatus and incubated for 3 h, after which the chamber fluid was collected for analysis (Figure 2A). As illustrated by the colony counts on the Petri dishes after 24 h shown in Figure \$12 (Supporting Information), the modified bacteria demonstrated the ability to transverse the agar layer from the upper chamber to the lower chamber, indicating that their migratory capacity remained intact. However, the results revealed that there was almost no bacterial migration in the experimental group exposed to NIR irradiation, likely because the photothermal effect resulted in bacterial inactivation. The fluorescence spectra presented in Figure 2B,C, which display the emission peaks of bacterial green fluorescent protein at 510 nm and those of AuNRs-Cy5.5 at ≈710 nm, further confirm that the engineered BL21 strain is capable of transporting loaded AuNRs through the agar layer, and this functionality can be precisely disrupted by NIR irradiation.

Previous studies have demonstrated that some facultative anaerobic bacteria exhibit an inherent ability to colonize the hypoxic TME of solid tumors in vivo. [46,47] In this section, we assessed the targeted colonization capability of engineered BL21 cells by establishing an in vitro 4T1 3D tumor cell spheroid model (TCS), which replicates the 3D structure and TME characteristics of tumors (Figure 2D). [48] As shown in Figure 2E, the CLSM images indicated that after a 6-h coincubation with TCSs, Au-DSF@CuS-BL21 ( $1.0 \times 10^9$  CFU mL<sup>-1</sup>) exhibited a pronounced fluorescent signal in the deep part of the TCSs. This observation suggested that Au-DSF@CuS-BL21 was capable of penetrating deeply into the TCSs. To investigate whether engineered bacteria carrying the Au-DSF could subsequently infiltrate tumor cells

to different conditions for 6 h (dead bacteria stained red; live bacteria stained green) (scale bar:  $50 \, \mu m$ ). H) Photothermal images of Au-DSF@CuS-BL21 (BL21:  $1.0 \times 10^9$  CFU mL $^{-1}$ , AuNRs:  $10.8 \, \text{mg L}^{-1}$ ) exposed to an 808 nm laser at varying intensities. I) Photothermal conversion curves of PBS (a), BL21 (b), PDA@BL21 (c), PDA@CuS-BL21 (d), and Au-DSF@CuS-BL21 (e) ( $1.0 \times 10^9$  CFU mL $^{-1}$ ) exposed to an 808 nm NIR laser ( $1.5 \, \text{W cm}^{-2}$ ). J) Thermal conversion efficiency diagram K) thermal cycling of Au-DSF@CuS-BL21 (BL21:  $1.0 \times 10^9$  CFU mL $^{-1}$ , AuNRs:  $10.8 \, \text{mg L}^{-1}$ ) exposed to an 808 nm laser ( $1.5 \, \text{W cm}^{-2}$ ).

www.advancedsciencenews.com

16163028, 0, Downloaded from https://advanced.onlinelibrary.wiley.com/doi/10.1002/adfm.202519382 by Hangzhou Normal University, Wiley Online Library on [10/11/2025]. See the Terms

and Conditions (https://onlinelibrary.wiley.com/tern

and-conditions) on Wiley Online Library for rules of use; OA articles are governed by the applicable Creative Commons License

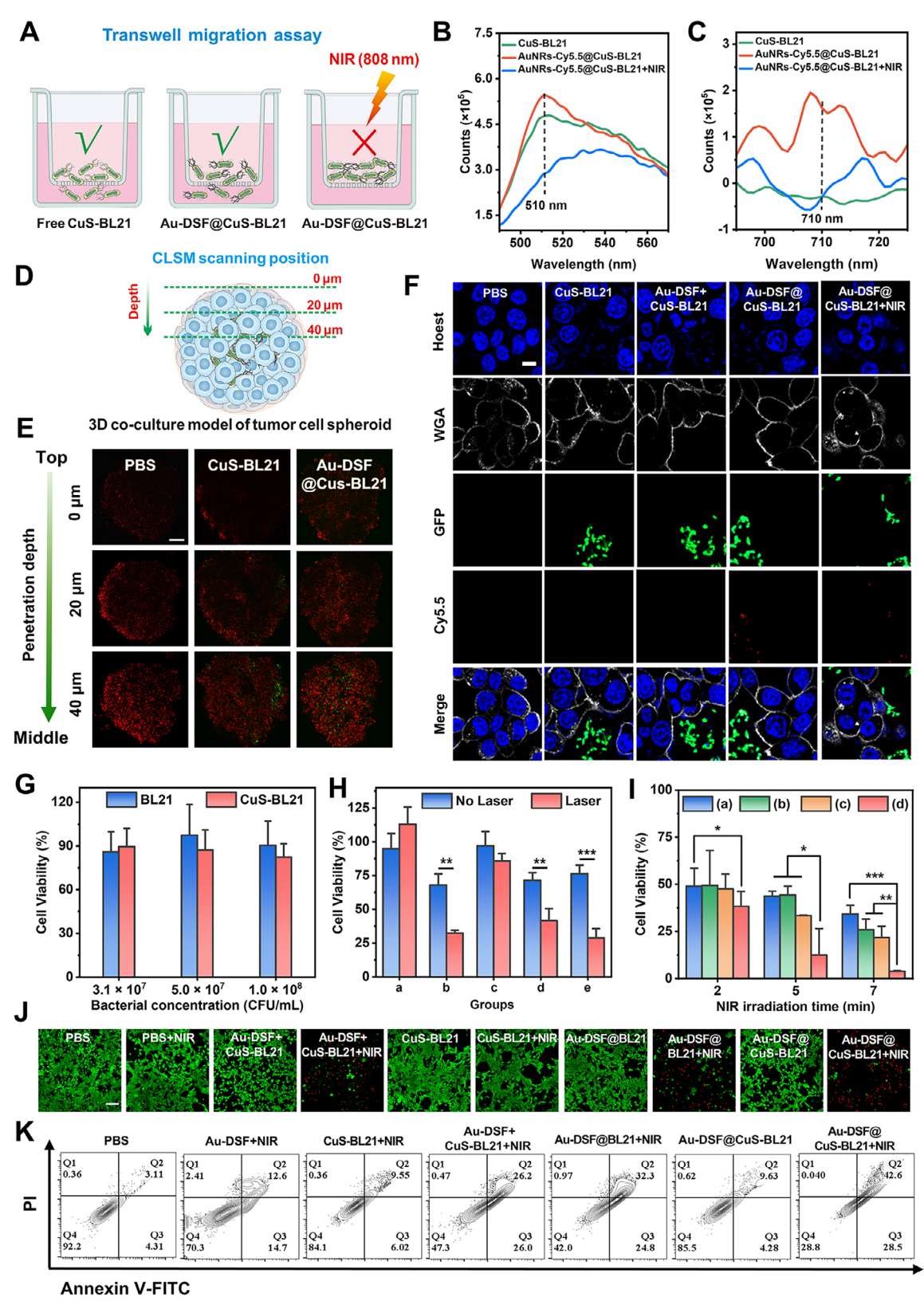


Figure 2. A) Schematic of the transwell assay to investigate bacterial penetration behavior. Fluorescence spectra of (B) GFP and (C) AuNRs-Cy5.5 in the chamber fluid at the 3-h mark of the transwell assay. D) Schematic diagram illustrating the scanning position of a 3D tumor cell spheroid with the colocalization of engineered bacterial formulations. E) CLSM images displaying the distribution of fluorescently engineered BL21 formulations within 4T1 tumor spheroids (20 μm per step, scale bar: 100 μm). F) Engineered bacterial cell colocalization CLSM images after treatment with various therapeutic

1616928, 0, Downloaded from https://advanced.onlinelibrary.wiley.com/doi/10.1002adfm.202519382 by Hangzhou Normal University, Wiley Online Library on [10.11.12025]. See the Terms and Conditions (https://onlinelibrary.wiley.com/terms-and-conditions) on Wiley Online Library for rules of use; OA articles are governed by the applicable Ceravive Commons

upon reaching them, we stained the cell membranes and nuclei. CLSM analysis, as shown in Figure 2F, revealed that the bacteria did not penetrate the cells; however, the Au-DSF@CuS-BL21 with NIR irradiation (Au-DSF@CuS-BL21+NIR)-treated group displayed red fluorescence within the cells. This observation suggested that the Au-DSF was successfully released and subsequently internalized by the 4T1 cells through endocytosis triggered by NIR irradiation.

The cytotoxicity of the BL21-based formulations was evaluated in the 4T1 cell line. As illustrated in Figure S13 (Supporting Information), it is evident that Cu2+ and DSF individually do not exhibit significant toxicity to cells. However, when co-cultured with free Cu<sup>2+</sup> and DSF, cell viability decreased sharply to 57%, indicating that the rapidly formed CuET enhances cellular toxicity and independently confirms its therapeutic effect. Notably, with NIR irradiation, the cell survival rate in the group treated with Cu<sup>2+</sup> + Au-DSF dropped to only 12%, demonstrating that NIR irradiation can further enhance the therapeutic efficacy of the nanocomposites. The biocompatibility of CuS-BL21 was subsequently assessed through in vitro experiments. As illustrated in Figure 2G, the cell viability following incubation with CuS-BL21 did not exhibit a significant decrease compared to cells treated with the blank BL21 in the absence of NIR irradiation, thereby demonstrating favorable in vitro biosafety. A bacterial concentration of  $5.0 \times 10^7$  CFU mL<sup>-1</sup> was subsequently used for further experiments. As shown in Figure 2H and Figure S14A (Supporting Information), all the experimental groups exhibited relatively low toxicity in the absence of NIR irradiation. However, upon the application of laser irradiation, a marked increase in cytotoxicity was observed across most experimental groups, particularly in the free drug (Au-DSF+CuS-BL21)-treated group and the Au-DSF@CuS-BL21-treated group, which demonstrated the most pronounced toxicity. This increase in cytotoxicity may be attributed to the activation and acceleration of CuET generation induced by the photothermal effect. Notably, NIR irradiation did not significantly augment the cellular toxicity of free CuS-BL21. This result can be explained by the fact that CuS-BL21 is present in the extracellular space, which hinders its ability to effectively induce cell death, as the photothermal effects of CuS are not readily accessible to the cells. Furthermore, we found that cytotoxicity was positively correlated with the concentration of Au-DSF@CuS-BL21, laser intensity, and irradiation duration under the same conditions (Figure 21; Figure S14B,C, Supporting Information).

The live/dead cell double-staining technique was employed to visually assess the cytotoxic effects of various treatments on 4T1 cells, with live cells indicated by green fluorescence and dead cells indicated by red fluorescence. As shown in Figure 2J, both the PBS control group (a) and the laser-only group (b) exhibited pronounced green fluorescence, indicating minimal adverse effects of the laser on 4T1 cells under experimental conditions. Conversely, treatment with Au-DSF@BL21+NIR resulted in obvi-

ous cell death, as evidenced by extensive red areas. Furthermore, larger areas of cell death were observed in the Au-DSF+CuS-BL21+NIR group and the Au-DSF@CuS-BL21+NIR group than in the other groups, which aligns with the findings from the MTT assay. These results underscore the potent capacity of Au-DSF@CuS-BL21 to induce tumor cell death upon activation by NIR irradiation. The activation of apoptotic mechanisms by the engineered bacteria in 4T1 cells was subsequently further examined through flow cytometry analysis. The findings in Figure 2K revealed that, in comparison with those in the PBS group, the 4T1 cells in the CuS-BL21+NIR-treated group exhibited increased apoptosis, corroborating the CLSM staining results for live/dead cells. Notably, Au-DSF@CuS-BL21 did not elicit additional adverse reactions upon light exposure, with 71.1% of the apoptotic cells (early apoptotic + late apoptotic) undergoing apoptosis following laser irradiation. These data indicate that the engineered bacterial formulations effectively induced apoptosis at both the early and late stages after induction by NIR irradiation, thereby significantly inhibiting the proliferation of 4T1 tumor cells.

### 2.5. Au-DSF@CuS-BL21-Mediated Combination Therapy

BALB/c mice bearing 4T1 tumors were employed as experimental animal models to investigate the tumor-targeting capability of Au-DSF@CuS-BL21, following a protocol approved by the Animal Care Committee of Hangzhou Normal University (No. HSD-20231201-02) (Figure 3). Initially, to ensure the biosafety of the engineered bacteria, a comprehensive hemolysis assay was performed. The findings indicated that, relative to the positive control, the engineered BL21 strain displayed favorable blood compatibility, underscoring its considerable potential for application in in vivo studies (Figure \$15, Supporting Information). Then, to facilitate visualization of the material's signal, the AuNRs were conjugated with Cy5.5-SH. Various formulations, including PBS, CuS-BL21+Au-DSF, and Au-DSF@CuS-BL21, were subsequently administered to the mice via tail vein injection, followed by fluorescence imaging at predetermined time points. As shown in Figure 3B, the fluorescence signal from free AuNRs showed minimal accumulation at the tumor site. In contrast, the AuNRs associated with the BL21 strain demonstrated significant enrichment at the tumor site at the 8-h mark, along with a pronounced retention effect, suggesting that BL21 increases the accumulation of the AuNRs within the tumor. To further substantiate the targeting ability of the bacteria, anatomical sections were stained with Au-DSF@CuS-BL21 8 h after intravenous injection. As shown in Figure 3C, the presence of the Au-DSF@CuS-BL21 group was evident in the tumor sections, marked by the green fluorescence of the engineered bacteria, indicating the targeted motility of the engineered bacteria toward the tumor.

Then, the in vivo photothermal effects of various experimental treatments were assessed in 4T1 tumor-bearing BALB/c mice.

agents for 6 h (scale bar:  $10 \, \mu m$ ). Cell viability of 4T1 cells after coculture for 24 h with (G) BL21 or CuS-BL21 without NIR irradiation; H) PBS (a), CuS-BL21+Au DSF (b), CuS-BL21 (c), Au-DSF@BL21 (d), or Au-DSF@CuS-BL21 (e) with or without laser irradiation ( $1.0 \, W \, cm^{-2}$ ); and I) Au-DSF@CuS-BL21 with different Au-DSF concentrations ((a)  $1.0 \, mg \, L^{-1} \, Au$ -DSF, (b)  $3.0 \, mg \, L^{-1} \, Au$ -DSF, (c)  $5.0 \, mg \, L^{-1} \, Au$ -DSF, (d)  $7.0 \, mg \, L^{-1} \, Au$ -DSF) under NIR ( $1.0 \, W \, cm^{-2}$ ) exposure for different times (n=3). J) Quantitative analysis of CLSM images showing live/dead staining of 4T1 cells subjected to different treatments for 24 h (scale bar,  $100 \, \mu m$ ). K) Flow cytometry analysis of apoptosis in annexin V-FITC/PI-stained 4T1 cells subjected to different treatments for  $12 \, h \, p^2 \, 0.05$ ; p = 0.05; p = 0.05; p = 0.00; p = 0.00;

and-conditions) on Wiley Online Library for rules of use; OA articles are governed by the applicable Creative Commons License

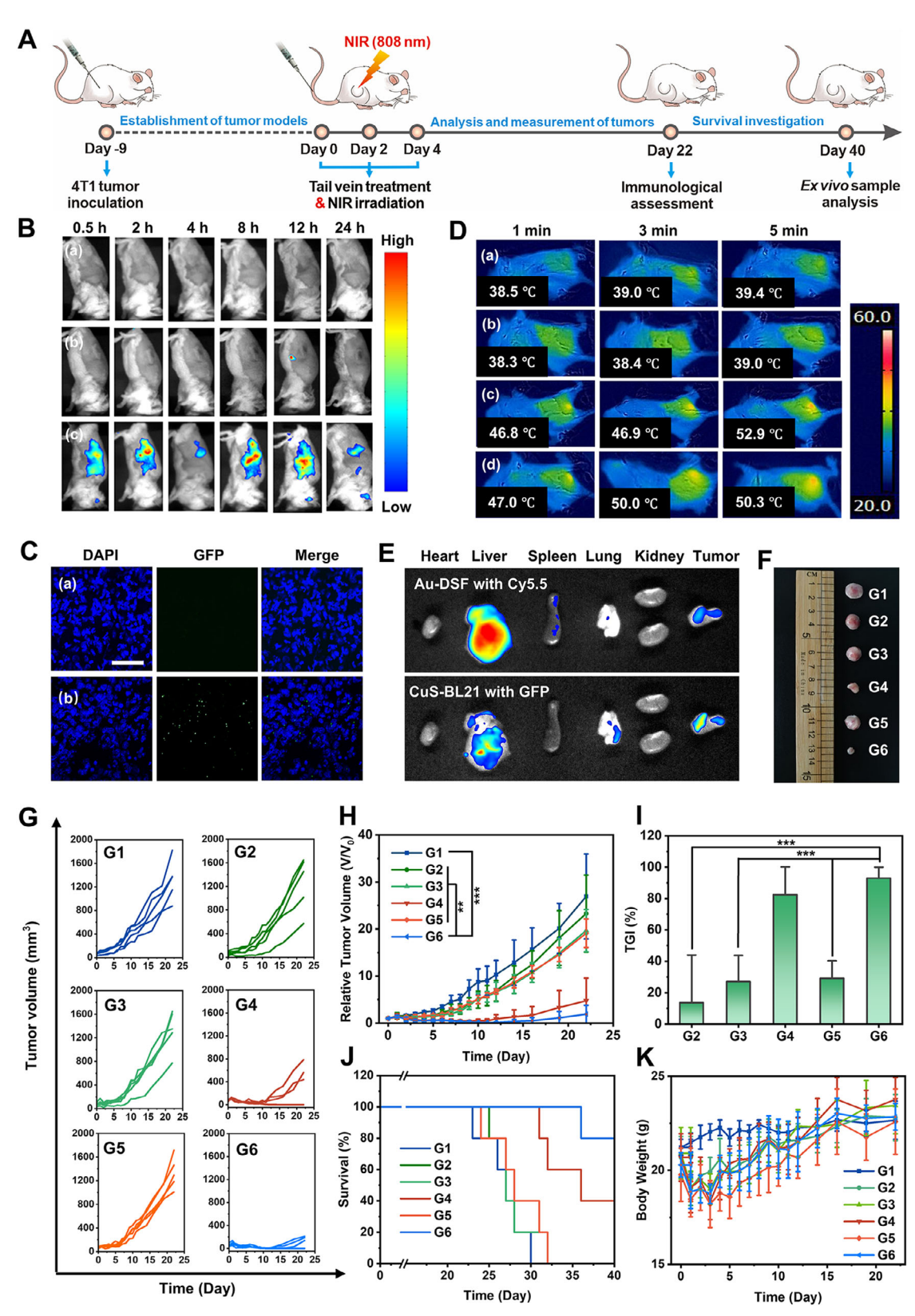


Figure 3. A) Schematic diagram of the experimental design and time course for the Au-DSF@CuS-BL21 antitumor treatments. B) In vivo bioluminescence imaging of subcutaneous 4T1 tumor-bearing BALB/c mice at different intervals after treatment with PBS (a), free Au-DSF + CuS-BL21 (b), or Au-DSF@CuS-BL21 (c). C) CLSM images of tumor slices after injection of PBS (a) or Au-DSF@CuS-BL21 (b) (scale bar, 50 μm) for 8 h. D) Thermal images of tumor-bearing mice exposed to a 1.0 W cm<sup>-2</sup> laser for varying irradiation durations after treatment with free CuS-BL21+Au-DSF (a), CuS-BL21

www.advancedsciencenews.com



16163028, 0, Downloaded from https://advacced.onlinelibrary.wiley.com/doi/10.1002/affm20251582 by Hangzbou Normal University, Wiley Online Library on [1011/2025]. See the Terms and Conditions (https://onlinelibrary.wiley.com/terms-and-conditions) on Wiley Online Library for rules of use; OA articles are governed by the applicable Centwise Commons

www.afm-journal.de

The mice were administered CuS-BL21+Au-DSF, CuS-BL21, Au-DSF@BL21, or Au-DSF@CuS-BL21 via tail vein injection. Eight hours after treatment, the tumor area was exposed to an NIR laser (808 nm, 1.0 W cm<sup>-2</sup>) for different durations (1, 3, or 5 min), and the resulting photothermal effects were recorded using an infrared thermal imaging camera. As illustrated in Figure 3D, the effectiveness of illumination for each group increased with increasing irradiation time. Among the groups, Au-DSF@CuS-BL21 exhibited the most significant photothermal effect, with the tumor temperature reaching 50.3 °C after 5 min of exposure, indicating superior photothermal performance in the mice (Figure \$16, Supporting Information). To further assess the biosafety of the NIR irradiation protocol (808 nm, 1.0 W cm<sup>-2</sup>, 5 min) on adjacent tissues, histopathological analysis was conducted on skin samples surrounding the tumor sites at 0 and 7 d post-treatment using Masson's trichrome staining. The findings demonstrated no notable pathological alterations, suggesting that this photothermal treatment regimen is comparatively safe for normal tissues (Figure \$17, Supporting Information). Thus, these findings suggest that CuS-BL21 may enhance the payload's delivery to the tumor site, facilitating the advancement of combined photothermal therapy.

Furthermore, the biodistribution and clearance dynamics of the engineered bacteria were evaluated following the treatment of Au-DSF@CuS-BL21. As shown in Figure 3E and Figure S18 (Supporting Information), although the surface fluorescence images of the tumor and major organs (the heart, liver, spleen, lung, and kidney) indicated a substantial accumulation of CuS-BL21 in the liver, fluorescent images of observed liver sections showed sparse green fluorescence localized in the liver region during the initial phase of treatment. At subsequent time points, the intensity of the green fluorescence markedly diminished, with the signal becoming nearly undetectable by day 7 post-treatment. Furthermore, it is noteworthy that, relative to the group not subjected to laser irradiation, the bacterial fluorescence signal within the liver was substantially reduced following laser-mediated tumor therapy. This observation may be attributed to the laser exposure impairing bacterial motility, thereby inhibiting their reentry into systemic circulation and subsequent hepatic accumulation. Complementary ICP analysis of the Au element corroborated these findings, as shown in Figure \$19 (Supporting Information). ICP analysis revealed that the Au concentration per unit of liver tissue was not high in the observation time points. In contrast, the Au-DSF@CuS-BL21 treatment group demonstrated a significant increase in Au accumulation in tumors compared to the free drug-treated group. This finding highlights the bacteria's hypoxia-targeting capability, which effectively enhances drug enrichment at the tumor site. Furthermore, following laser irradiation, the retention of gold nanoparticles within the tumor region was also improved on day 2. This effect is likely due to laser-induced bacterial lysis, which reduces bacterial migration and thereby promotes greater accumulation in the tumor area.

To further evaluate the effects of tumor treatment, female BALB/c mice with 4T1 tumors (60-80 mm<sup>3</sup>) were randomly divided into six groups: PBS (G1), CuS-BL21+Au-DSF+NIR (G2), CuS-BL21+NIR (G3), Au-DSF@BL21+NIR (G4), Au-DSF@CuS-BL21 (G5), and Au-DSF@CuS-BL21+NIR (G6). Treatments were administered via the tail vein on days 0, 2, and 4, followed by NIR laser exposure (808 nm, 1.0 W cm<sup>-2</sup>, 5 min) at the tumor site after 8 h of each treatment. Tumor size was measured using calipers at the set time points, and the body weights of the mice were recorded to monitor their survival. As shown in Figure 3F-H, the average tumor volume in the PBS group increased sharply, reaching ≈2000 mm<sup>3</sup> by day 22. Compared with the PBS group, the free drug-treated group (G2) presented a slight tumor suppressive effect (TGI: 13.5%). These outcomes arise from the inability of free drugs to accumulate at the tumor site in a synchronized and effective manner, hindering the ability of NIR irradiation to achieve optimal therapeutic results. The Au-DSF@BL21 with laser irradiation-treated group (G4) presented a significant reduction in tumor growth during the initial treatment phase, but this effect diminished by day 13. This decline was due to the absence of CuS nanoparticles in the G4 group, which prevented the effective formation of highly toxic CuET with DSF released from the AuNRs, leading to a limited tumor inhibitory effect. The G5 group, which did not receive laser treatment, also exhibited poor antitumor effects due to the absence of the combined therapeutic benefits of PTT. In contrast, the G6 group treated with Au-DSF@CuS-BL21+NIR achieved a remarkable tumor suppression rate of 92.9% (Figure 3I). This significant increase can be attributed to the photothermal interactions between the AuNRs and CuS-BL21 after exposure to the NIR laser, as well as the highly cytotoxic CuET formed through the interaction between the released DSF and the generated Cu<sup>2+</sup> upon NIR irradiation. Besides this, the enhanced immune response during the progression of therapy has also contributed to significant tumor inhibition, as discussed in the following section. Furthermore, the mouse survival rate of G6 was markedly improved compared to the other three groups within the observed 40 days also confirmed the above results (Figure 3]). Although the mice experienced a decrease in body weight during treatment, their weights quickly returned to normal within the monitored 22 days, indicating that the engineered BL21 is a safe therapeutic vehicle for cancer therapy (Figure 3K).

To assess the induction of the immune response in vivo through immunogenic cell death (ICD) and bacterial thermolytic antigens during treatment, we investigated the maturation of dendritic cells (DCs), T-cell infiltration, and the polarization of M1 macrophages within tumors subjected to various treatment modalities. Briefly, tumor tissue was harvested at 12 d posttreatment and subsequently analyzed by flow cytometry. Figure 4A,D demonstrate that the mature DC population in tumors from mice treated with Au-DSF@CuS-BL21+NIR (G6) was significantly higher, being 2.2 times greater than that in the PBS group

(b), Au-DSF@BL21 (c), and Au-DSF@CuS-BL21 (d). E) Luminescence images of the heart, liver, spleen, lung, and kidney after treatment with Au-DSF-Cy5.5@CuS-BL21 for 24 h. F) Representative photographs of tumors on mice after various treatments. G) Quantification of individual tumor growth curves, H) RTV results, I) mouse body weights, and K) TGI rates of mice subjected to different treatments for 22 d (n = 5). J) Survival rates of mice after different treatments for 40 d (n = 5). G1: PBS, G2: free CuS-BL21+Au-DSF+NIR, G3: CuS-BL21+NIR, G4: Au-DSF@BL21+NIR, G5: Au-DSF@CuS-BL21, G6: Au-DSF@CuS-BL21+NIR, G7: Au-DS

www.advancedsciencenews.com

www.afm-journal.de

16163028, 0, Downloaded from https://advanced.onlinelibrary.wiley.com/doi/10.1002/adfm.202519382 by Hangzhou Normal University, Wiley Online Library on [10/11/2025]. See the Terms and Conditions (https://onlinelibrary.wiley.com/ten

conditions) on Wiley Online Library for rules of use; OA articles are governed by the applicable Creative Commons License

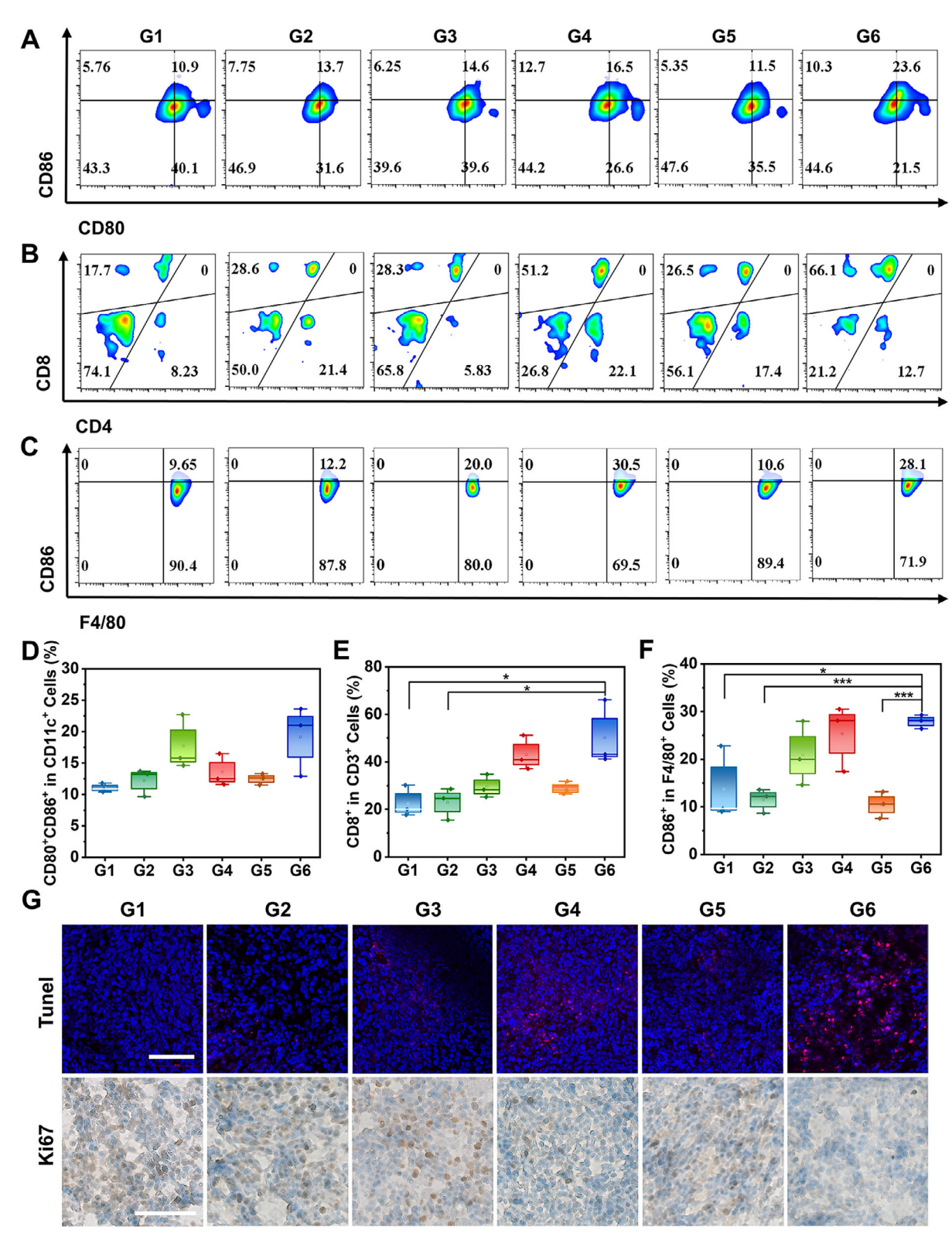


Figure 4. A) Representative flow cytometry analysis of mature dendritic cells (CD80+CD86+CD11c+). B) Flow cytometry analysis of CD8+ and CD4+ T cells (gated on CD3+ T cells) in tumors after different treatments. C) Representative flow cytometry image of M1 macrophages (CD80+F4/80+). Proportion of (D) mature dendritic cells, E) tumor-infiltrating CD8+ T cells, and F) tumor-infiltrating M1 macrophages in treated tumors (n=3). H) Ex vivo TUNEL assay and Ki-67 immunohistochemical staining of 4T1 tumors after treatments with various therapeutic agents for 12 d (scale bar, 100  $\mu$ m). G1: PBS, G2: CuS-BL21+Au-DSF+NIR, G3: CuS-BL21+NIR, G4: Au-DSF@BL21+NIR, G5: Au-DSF@CuS-BL21, G6: Au-DSF@CuS-BL21+NIR.  $^*p < 0.05$ ;  $^**^*p < 0.001$ .

ADVANCED
FUNCTIONAL
MATERIALS

(G1), 1.7 times greater than in the CuS-BL21+Au-DSF+NIR group (G2), 1.6 times greater than in the CuS-BL21+NIR group (G3), and 1.5 times greater than in the Au-DSF@BL21+NIR group (G4). Not only that, the population of both CD8+ T cells (Figure 4B,E) and M1-type macrophages (Figure 4C,F) in the Au-DSF@CuS-BL21+NIR (G6) group also exhibited the most significant increase in frequency compared to the other treated groups. These findings suggest that this combinatorial therapeutic approach, which utilizes engineered BL21, can significantly enhance the DC maturation and stimulate tumor-specific immune responses, leading to improved antitumor activity.

After treatment, the tumor tissues were collected, weighed, and subjected to histomorphological and immunohistochemical analyses. The results of the TUNEL assay, illustrated in Figure 4G, indicated that the combination of Au-DSF@CuS-BL21 and NIR effectively induced apoptosis in tumor cells. Additionally, Ki-67 staining demonstrated that this combination significantly decreased the number of proliferating cells. Hematoxylin and eosin (H&E) staining further confirmed that the Au-DSF@CuS-BL21 and laser treatment achieved maximal elimination of tumor cells. To assess the biosafety of the engineered bacteria, we conducted pathological examinations of H&E-stained primary organs in the mice (heart, liver, spleen, lung, kidney, etc.). As depicted in Figure S20 (Supporting Information), the pathological analysis of tissue sections from these organs across all groups revealed a normal tissue architecture with no significant pathological alterations, such as hemorrhage or inflammatory infiltration. These findings suggest that Au-DSF@CuS-BL21 has favorable biosafety characteristics in vivo.

#### 3. Conclusion

In summary, the present study concentrated on the genetic modification of an *E. coli* strain to biosynthesize CuS nanoparticles, which were subsequently integrated with DSF-loaded AuNRs to develop an engineered bacterial nanocomposite system designated as Au-DSF@CuS-BL21 for effectively targeted prodrug delivery and increased antitumor efficacy. The bacterial membrane functioned as a protective barrier, preventing the premature formation and release of the toxic CuET complex during circulation, thereby ensuring bacterial viability and minimizing drug leakage. The principal findings demonstrated that the engineered bacteria retained their functional activity while enhancing tumor targeting and penetration capabilities. Activation via NIR irradiation induced photothermal bacterial lysis, resulting in the release of CuS and DSF, which subsequently formed the CuET complex, thereby augmenting antitumor efficacy through the stimulation of the innate immune response. The research underscores the potential for improved biosafety in genetically modified bacteria and the effective compartmentalized delivery of prodrugs, contributing to enhanced cancer treatment strategies.

# **Supporting Information**

Supporting Information is available from the Wiley Online Library or from the author.

# Acknowledgements

Y.L., L.R., and H.L. contributed equally to this work. This work was supported by the National Natural Science Foundation of China (Nos. 52473127, 22275046, 22161142015), the National Key R&D Program of China (No. 2020YFA0908500), the Hangzhou Leading Innovation and Entrepreneurship Team Project (No. TD2022001), and the Interdisciplinary Research Project of Hangzhou Normal University (2025JCXK02).

#### **Conflict of Interest**

The authors declare no conflict of interest.

# **Data Availability Statement**

The data that support the findings of this study are available from the corresponding author upon reasonable request.

#### **Keywords**

biosynthesized CuS nanoparticles, cancer therapy, disulfiram, engineered bacteria, gold nanorods, prodrug delivery

Received: July 26, 2025 Revised: October 6, 2025 Published online: 16163028, 0, Downloaded from https://advanced.onlinelibrary.wiley.com/doi/10.1002/adfm.202519382 by Hangzhou Normal University, Wiley Online Library on [10/1/2025]. See the Terms and Conditions (https://onlinelibrary.wiley.com/term/terms/

and-conditions) on Wiley Online Library for rules of use; OA articles are governed by the applicable Creative Commons

- M. Yarchoan, B. A. Johnson, E. R. Lutz, D. A. Laheru, E. M. Jaffee, Nat. Rev. Cancer 2017, 17, 209.
- [2] I. Godet, Y. J. Shin, J. A. Ju, I. C. Ye, G. Wang, D. M. Gilkes, *Nat. Commun.* 2019, 10, 4862.
- [3] A. Bhardwaj, M. C. Panepinto, B. Ueberheide, B. G. Neel, *Nature* 2024, 637, 470.
- [4] J. Pouysségur, F. Dayan, N. M. Mazure, Nature 2006, 441, 437.
- [5] J. Li, B. Hu, Z. Chen, J. Li, W. Jin, Y. Wang, Y. Wan, Y. Lv, Y. Pei, H. Liu, Z. Pei, Chem. Sci. 2024, 15, 765.
- [6] S. Zhou, C. Gravekamp, D. Bermudes, K. Liu, Nat. Rev. Cancer 2018, 18, 727.
- [7] C. R. Gurbatri, N. Arpaia, T. Danino, Science 2022, 378, 858.
- [8] X. Lou, Z. Chen, Z. He, M. Sun, J. Sun, Nano-Micro Lett. 2021, 13,
- [9] C. Wang, L. Zhong, J. Xu, Q. Zhuang, F. Gong, X. Chen, H. Tao, C. Hu, F. Huang, N. Yang, J. Li, Q. Zhao, X. Sun, Y. Huo, Q. Chen, Y. Zhao, R. Peng, Z. Liu, Nat. Biomed. Eng. 2024, 8, 561.
- [10] L. T. Geller, T. Danino, O. H. Jonas, N. Shental, D. Nejman, N. Gavert, Y. Zwang, Z. A. Cooper, K. Shee, C. A. Thaiss, A. Reuben, J. Livny, R. Avraham, D. T. Frederick, M. Ligorio, K. Chatman, S. E. Johnston, C. M. Mosher, A. Brandis, G. Fuks, C. Gurbatri, V. Gopalakrishnan, M. Kim, M. W. Hurd, M. Katz, J. Fleming, A. Maitra, D. A. Smith, M. Skalak, J. Bu, et al., Science 2017, 357, 1156.
- [11] W. Song, A. C. Anselmo, L. Huang, Nat. Nanotechnol. 2019, 14, 1093.
- [12] H. Xu, S. Xiong, Y. Chen, Q. Ye, N. Guan, Y. Hu, J. Wu, Adv. Mater. 2023, 35, 2303357.
- [13] S. Chowdhury, S. Castro, C. Coker, T. E. Hinchliffe, N. Arpaia, T. Danino, *Nat. Med.* 2019, 25, 1057.
- [14] T. J. Park, S. Y. Lee, N. S. Heo, T. S. Seo, Angew. Chem., Int. Ed. 2010, 49, 7019.
- [15] Y. Park, Z. Eyal, P. Pekker, D. M. Chevrier, C. T. Lefèvre, P. Arnoux, J. Armengaud, C. L. Monteil, A. Gal, M. Pósfai, D. Faivre, Adv. Sci. 2022, 9, 2203444.

16163028, 0, Downloaded from https://advanced.onlinelibrary.wiley.com/doi/10.1002/adfm.202519382 by Hangzhou Normal University, Wiley Online Library on [10/11/2025]. See the Terms

and Conditions

https://onlinelibrary.wiley

on Wiley Online Library for rules of

use; OA articles

s are governed by the applicable Creative Commons

- [16] P. Song, X. Han, X. Li, Y. Cong, Y. Wu, J. Yan, Y. Wang, X. Wang, Z. Mu, L. Wang, X. Li, H. Zhang, Mater. Horiz. 2023, 10, 2927.
- [17] Y. E. Chen, D. Bousbaine, A. Veinbachs, K. Atabakhsh, A. Dimas, V. K. Yu, A. Zhao, N. J. Enright, K. Nagashima, Y. Belkaid, M. A. Fischbach, Science 2023, 380, 203.
- [18] W. Wu, Y. Pu, S. Gao, Y. Shen, M. Zhou, H. Yao, J. Shi, Nano-Micro Lett. 2022, 14, 220.
- [19] L. Wang, Z. Cao, M. Zhang, S. Lin, J. Liu, Adv. Mater. 2021, 34, 2106669
- [20] J. Nemunaitis, C. Cunningham, N. Senzer, J. Kuhn, J. Cramm, C. Litz, R. Cavagnolo, A. Cahill, C. Clairmont, M. Sznol, Cancer Gene Ther. 2003, 10, 737.
- [21] R. W. Kasinskas, N. S. Forbes, Biotechnol. Bioeng. 2006, 94, 710.
- [22] Y. Ma, Y. Hu, H. Liu, X. Li, Y. Li, Y. Zhao, Q. Zhang, Z. Zhang, Q. Leng, L. Luo, L. Li, Y. Dai, G. Chen, J. Zhang, Z. Li, Adv. Mater. 2024, 36, 2405930.
- [23] X. Dai, Z. Liu, X. Zhao, K. Guo, X. Ding, F. J. Xu, N. Zhao, Adv. Mater. 2024, 36, 2407927.
- [24] K. Yang, K. Ma, M. Yang, Y. Lv, Y. Pei, Z. Pei, Chem. Commun. 2023, 59, 3779.
- [25] L. Hou, Y. Liu, W. Liu, M. Balash, H. Zhang, Y. Zhang, H. Zhang, Z. Zhang, Acta Pharm. Sin. B 2021, 11, 2016.
- [26] W. Wu, L. Yu, Q. Jiang, M. Huo, H. Lin, L. Wang, Y. Chen, J. Shi, J. Am. Chem. Soc. 2019, 141, 11531.
- [27] X. Man, W. Li, M. Zhu, S. Li, G. Xu, Z. Zhang, H. Liang, F. Yang, Angew. Chem., Int. Ed. 2024, 63, 202411846.
- [28] Z. Skrott, M. Mistrik, K. K. Andersen, S. Friis, D. Majera, J. Gursky, T. Ozdian, J. Bartkova, Z. Turi, P. Moudry, M. Kraus, M. Michalova, J. Vaclavkova, P. Dzubak, I. Vrobel, P. Pouckova, J. Sedlacek, A. Miklovicova, A. Kutt, J. Li, J. Mattova, C. Driessen, Q. P. Dou, J. Olsen, M. Hajduch, B. Cvek, R. J. Deshaies, J. Bartek, Nature 2017, 552, 194.
- [29] Y. Wang, Z. Chen, J. Li, Y. Wen, J. Li, Y. Lv, Z. Pei, Y. Pei, Adv. Sci. 2023, 11, 2306178.
- [30] J. Zhou, Z. Cao, N. Panwar, R. Hu, X. Wang, J. Qu, S. C. Tjin, G. Xu, K.-T. Yong, Coordin. Chem. Rev. 2017, 352, 15.
- [31] P. Kesharwani, R. Ma, L. Sang, M. Fatima, A. Sheikh, M. A. S. Abourehab, N. Gupta, Z.-S. Chen, Y. Zhou, Mol. Cancer 2023, 22, 98.

- [32] J. Zheng, X. Cheng, H. Zhang, X. Bai, R. Ai, L. Shao, J. Wang, Chem. Rev. 2021, 121, 13342.
- [33] J. Huang, J. Zhou, J. Zhuang, H. Gao, D. Huang, L. Wang, W. Wu, Q. Li, D.-P. Yang, M.-Y. Han, ACS Appl. Mater. Interfaces 2017, 9, 36606.
- [34] J. Ma, N. Li, J. Wang, Z. Liu, Y. Han, Y. Zeng, Exploration 2023, 3, 20220161.
- [35] B. Koul, A. K. Poonia, D. Yadav, J.-O. Jin, Biomolecules 2021, 11,
- [36] S. Zhang, J. Yang, J. Luo, J. Zhang, M. Huang, K. Tan, G. Chen, Q. Xing, H. F. Kwok, Z. Dai, J. Geng, Angew. Chem., Int. Ed. 2025, 13, 202504936.
- [37] D. K. Gahlot, N. Taheri, D. R. Mahato, M. S. Francis, Sci. Rep. 2020, 10, 20327.
- [38] Y. Choi, T. J. Park, D. C. Lee, S. Y. Lee, Proc. Natl. Acad. Sci. USA 2018, 115 5944
- [39] W.-Z. Qiu, H.-C. Yang, Z.-K. Xu, Adv. Colloid Interface Sci. 2018, 256,
- [40] L. Wang, J. Liu, Acc. Chem. Res. 2024, 57, 945.
- [41] X. Li, J. F. Lovell, J. Yoon, X. Chen, Nat. Rev. Clin. Oncol. 2020, 17,
- [42] N. Brkovic, L. Zhang, J. N. Peters, S. Kleine-Doepke, W. J. Parak, D. Zhu, Small 2020, 16, 2003639.
- [43] J. Ji, F. Ma, H. Zhang, F. Liu, J. He, W. Li, T. Xie, D. Zhong, T. Zhang, M. Tian, H. Zhang, H. A. Santos, M. Zhou, Adv. Funct. Mater. 2018, 28, 2003639.
- [44] J. Xu, B. Zheng, S. Zhang, X. Liao, Q. Tong, G. Wei, S. Yu, G. Chen, A. Wu, S. Gao, Y. Qian, Z. Xiao, W. Lu, Adv. Funct. Mater. 2021, 31,
- [45] L. Xu, G. Tong, Q. Song, C. Zhu, H. Zhang, J. Shi, Z. Zhang, ACS Nano 2018, 12, 6806.
- [46] H. Shen, C. Zhang, S. Li, Y. Liang, L. T. Lee, N. Aggarwal, K. S. Wun, J. Liu, S. P. Nadarajan, C. Weng, H. Ling, J. K. Tay, D. Y. Wang, S. Q. Yao, I. Y. Hwang, Y. S. Lee, M. W. Chang, Nat. Commun. 2024, 15, 4343.
- [47] Z. Geng, Z. Cao, R. Liu, K. Liu, J. Liu, W. Tan, Nat. Commun. 2021, 12, 6584
- [48] C. R. Thoma, M. Zimmermann, I. Agarkova, J. M. Kelm, W. Krek, Adv. Drug Delivery Rev. 2014, 69-70, 29.